International Journal of Solids and Structures 46 (2009) 1334–1344

Contents lists available at ScienceDirect

International Journal of Solids and Structures

journal homepage: www.elsevier.com/locate/ijsolstr

Computational modeling of surface phenomena in soft-wet materials

Ilinca Stanciulescu [a,*], John E. Dolbow [b], Stefan Zauscher [c]

[a] Department of Civil and Environmental Engineering, University of Illinois at Urbana Champaign, Urbana, IL 61801, USA
[b] Department of Civil and Environmental Engineering, Duke University, Durham, NC 27708, USA
[c] Department of Mechanical Engineering and Materials Science, Duke University, Durham, NC 27708, USA

ARTICLE INFO

Article history:
Received 9 June 2008
Received in revised form 31 October 2008
Available online 17 November 2008

Keywords:
Finite element formulations
Mortar contact discretization
Tribological properties
Soft-wet materials
Hydrogels

ABSTRACT

We consider the problem of extracting tribological information from experimental observations of contact with soft-wet materials. Particular attention is placed on simulating the response of two rotating cylinders of soft specimens placed in frictional contact, with a variable coefficient of friction dependent on the relative sliding velocity. The bulk behavior is modeled by means of a finite deformation viscoelasticity formulation, with constitutive parameters taken to be representative of hydrogels. We focus on the modeling of the surface behavior and employ a mortar-finite element contact formulation. Through a series of numerical studies, we demonstrate the strong sensitivity of the results to the choice of interfacial constitutive parameters. The difficulties of extracting such parameters using only experimental data and approximate analytical expressions are also examined.

1. Introduction

Biological tissues and stimulus-responsive hydrogels fall under the broad class of "soft-wet" materials (Osada and Gong, 1999), possessing relatively small elastic moduli (~100 kPa) and being hydrated or functioning in solution. From a mechanical perspective, these materials are characterized by an ability to sustain large, finite strains, and typically exhibit a viscoelastic response to applied loads. In many applications of interest to engineers and material scientists, load transmission occurs through frictional contact. Unfortunately, a number of factors can make it difficult to accurately characterize the surface behavior of soft-wet materials using experimental measurements alone. In this paper, we discuss the salient issues in detail and demonstrate the utility of mortar-finite element methods for investigating tribological complexity in soft-wet materials.

Stimulus-responsive hydrogels and other soft, active materials exhibit large displacements in response to small changes in environmental stimuli. They have been used for a wide range of applications, including optical switches (Pardo-Yissar et al., 2001), drug carriers (Eichenbaum et al., 1999), and microfluidic control (Beebe et al., 2000). As new applications continue to emerge, so do theoretical models for their behavior. A review of much of the early theoretical work is provided by Onuki (1993). More recent models account for finite strains and explicit phase transitions (see, e.g. Dolbow et al., 2004), various chemo-electro-mechanical couplings (Bassetti et al., 2005; Li et al., 2007; Hong et al., 2008), and viscoelasticity (Korchagin et al., 2007).

Although most of the attention has been focused on the bulk response of these materials, researchers are beginning to examine the interesting tribological behavior of polymer gels. A few groups have studied frictional contact between gels and various surfaces (Baumberger et al., 2002; Gong et al., 1999; Chang et al., 2007). Tribological response in these materials can depend on a number of factors, including charge, surface pressure, and relative sliding velocity. Some have followed the work of Gong et al. (1999) and adapted rheometers for studying gel-on-gel contact, in part due to the ease with which the specimens can be placed in solution. For example, Chang et al. (2007) used a similar experiment to show dramatic, reversible changes in tribological response with gel phase state. The rheometer configuration allows for steady-state conditions to be reached, eliminating the role of time dependence in the bulk response while rotational sliding occurs on the surface. Such a decoupling can be difficult to secure with configurations that employ a cyclic translational motion of the two surfaces.

While the rheometer setup is very useful for tribological studies of soft-wet materials, it mostly provides a means for qualitative investigations of surface response. The configuration allows for the measurement of net torque and normal loads produced by the contact during rotational sliding. Because the relative sliding velocity is non-uniform over the surface, some hypothesis regarding the relationship between frictional force and sliding velocity is required to extract tribological information. For example, Gong et al. (1999) assumed a linear relationship with zero asymptote to extract the apparent coefficient of friction. These considerations help motivate the need for accompanying numerical studies to

* Corresponding author.
E-mail address: ilincas@illinois.edu (I. Stanciulescu).

0020-7683/$ - see front matter © 2008 Elsevier Ltd. All rights reserved.
doi:10.1016/j.ijsolstr.2008.11.007

investigate the validity of such assumptions and isolate quantitative aspects that are necessary for design.

Robust simulation of frictional contact between two deformable, viscoelastic materials with complex tribological response is not trivial. This is particularly true when the rheometer configuration is modeled and the goal is to obtain sufficient accuracy to discern between various constitutive laws on the surface. With finite element based discretizations, for example, the simulation of rotational sliding in three dimensions practically rules out classical node-to-surface constraint strategies. By comparison, the mortar-finite element strategies for frictional contact developed by Laursen and colleagues (McDevitt and Laursen, 2000; Yang et al., 2005) are much better suited for this situation. In this work, we adapt these strategies to handle frictional sliding with a rate dependent constitutive law for the surface. For the bulk response, many different choices of material models are available, as outlined above. We employ the finite-strain viscoelastic model of Reese and Govindjee, 1998, which contains most of the salient features that enable the modeling of the transmission of loads from surface contact to the bulk in soft-wet materials.

This paper is organized as follows. In the next section, we describe the rheometer configuration in detail and discuss the usual assumptions employed to extract apparent frictional coefficients. Section 3 then provides the problem formulation used to model the configuration, including the governing equations and bulk and interfacial constitutive models. In Section 4, we briefly describe the numerical discretization with finite element and mortar methods. Results from various numerical experiments are then presented and discussed in Section 5. Finally, we provide a summary and concluding remarks in the last section.

2. Rheometer experiments on hydrogels

In this section, we describe a simple experimental setup (Fig. 1) that has been used to investigate the surface response of gels and discuss the assumptions that can be employed to extract tribological information.

Two cylindrical gel samples are glued to the upper and lower plates of a rheometer and an axial load is applied that brings the two samples in contact. The diameter $d = 2R_{min}$ of the uppermost gel specimen is typically chosen to be slightly smaller than the diameter $D = 2R_{max}$ of the bottom specimen. This choice ensures full contact and minimizes edge effects.[1]

The setup is placed in solution such that both gel samples and plates are fully submerged. After the total vertical load is applied, the gap between the two plates is held fixed until the normal contact force N reaches steady state. Then the angular velocity ω of the bottom plate is increased in steps, using time intervals that are sufficiently long to allow for full relaxation. Torque and normal force data are recorded as a function of time.

The assumption is that the steady-state data at each value of ω can be used to isolate the relationship between surface friction and sliding velocity, since the time dependence of bulk terms has been eliminated. The extraction of useful information from a modeling perspective, however, typically involves the use of a number of simplifying assumptions. For example, Gong et al. (1999) assume that the friction per unit area at a distance r from the axis of rotation is linearly proportional to the sliding velocity. Further, assuming infinitesimal deformations, the frictional force f at any point on the gel surface is then given by $f = c\omega r$. The total frictional force F can then be approximated as

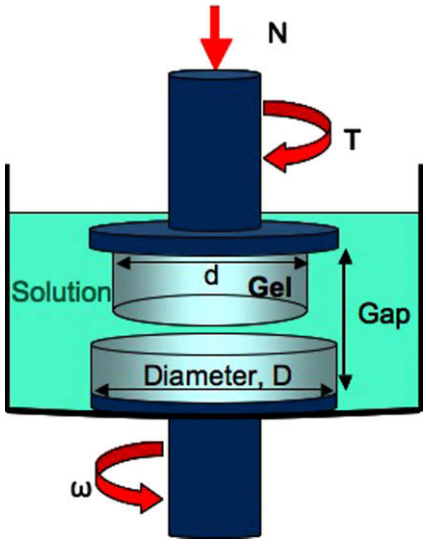

Fig. 1. Experimental setup for tribological measurements of gels.

$$F = \int_0^R 2\pi r f \, dr = \frac{2\pi}{3} c\omega R^3, \tag{2.1}$$

where R is the radius of the contact surface, which under the above assumptions is the radius of the top specimen, R_{min}. The corresponding torque is

$$T = \int_0^R 2\pi r f r \, dr = \frac{\pi}{2} c\omega R^4. \tag{2.2}$$

This allows one to express the frictional force in terms of the torque, as $F = 4T/3R$. An "apparent" coefficient of friction can then be calculated by dividing the frictional force by the axial load

$$\mu = \frac{F}{N} = \frac{4T}{3RN}. \tag{2.3}$$

Fig. 2 presents the evolution of the apparent coefficient of friction – estimated based on the relation (2.3) – during a set of experiments on hydrogels (for various initial axial loads N_i) that spanned four levels of angular velocity: 0.01, 0.1, 1 and 10 rad/s. A detailed description of the experimental data that was used in this study is presented in Chang et al. (2007). Clearly, an increase in the angular rotation ω gives rise to an increase in friction, which is at least self-consistent with the assumption that $f = c\omega r$. In the Sections that follow we will demonstrate, however, how drawing such inferences can be problematic.

3. Problem formulation

In this section, we describe a problem formulation suitable for modeling the experiment described in Section 2 and idealized in Fig. 1. In particular, we describe appropriate choices for the bulk and interfacial constitutive laws.

3.1. Finite deformation two body contact

Recognizing the potentially important role of large deformation with contact between two soft materials, we formulate the problem using finite-strain kinematics. Consider two bodies (as shown in Fig. 3), which in the reference configuration occupy the domains $\Omega^{(1)}$ and $\Omega^{(2)}$ and have boundaries $\Gamma^{(1)}$ and $\Gamma^{(2)}$. We consider only mechanical effects (i.e., force balance) and assume that inertial effects can be neglected. Subscripts u, σ and c indicate the segments on the boundary where displacements, tractions and contact con-

[1] We note that annular geometries are often impractical to use with soft materials due to the propensity for tearing.

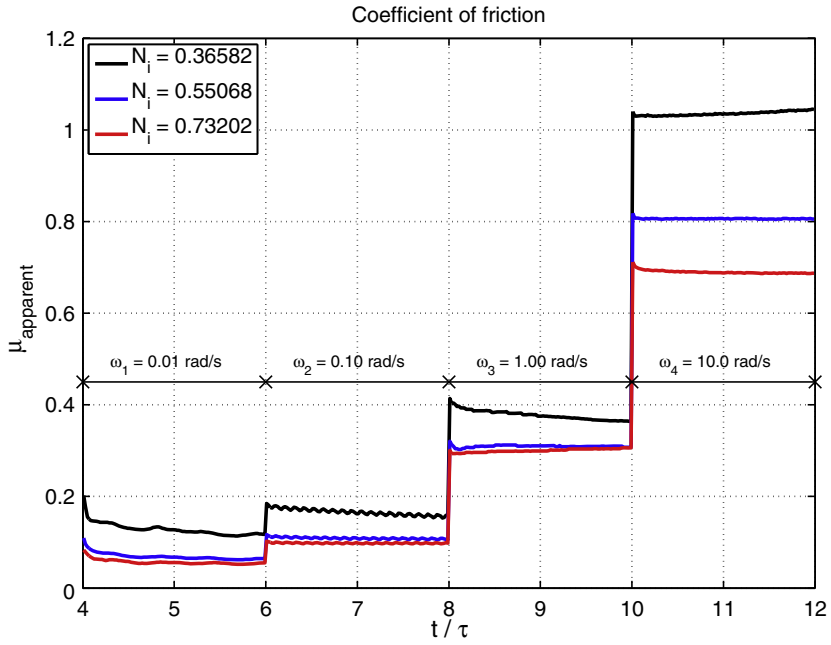

Fig. 2. Apparent μ estimated from measured torque and axial force data.

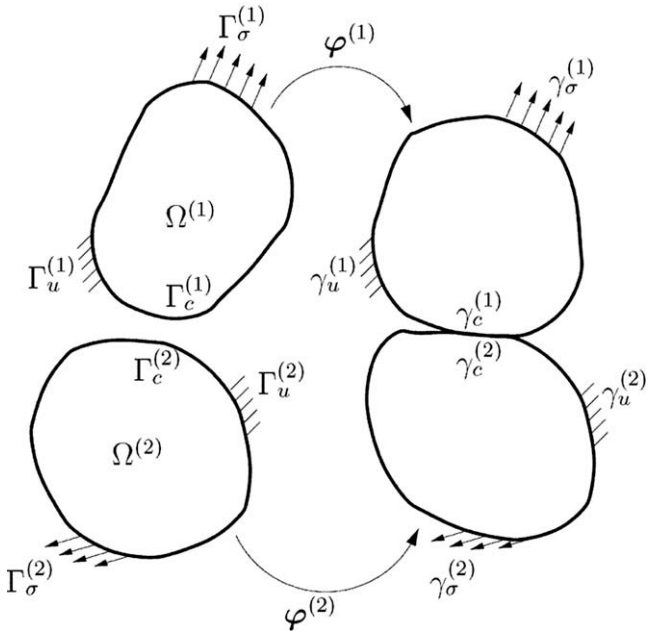

Fig. 3. Two body contact problem: Lagrangian description of the kinematics.

straints are prescribed. Denoting by $\boldsymbol{\varphi}^{(i)}$ a solution and by $\overset{*}{\boldsymbol{\varphi}}{}^{(i)}$ its variation, the spatial counterparts of the boundaries and domains are designated by $\gamma^{(i)}$ and $\boldsymbol{\varphi}^{(i)}(\Omega^{(i)})$, respectively. With these notations, one can express the virtual work

$$\begin{aligned} G(\boldsymbol{\varphi}, \overset{*}{\boldsymbol{\varphi}}) &:= \sum_{i=1}^{2} G^{(i)}(\boldsymbol{\varphi}^{(i)}, \overset{*}{\boldsymbol{\varphi}}{}^{(i)}) \\ &= \sum_{i=1}^{2} \left\{ \int_{\Omega^{(i)}} GRAD\overset{*}{\boldsymbol{\varphi}}{}^{(i)} : \boldsymbol{P}^{(i)}\, d\Omega - \int_{\Omega^{(i)}} \overset{*}{\boldsymbol{\varphi}}{}^{(i)} \cdot \boldsymbol{f}^{(i)}\, d\Omega \right. \\ &\quad \left. - \int_{\Gamma_\sigma^{(i)}} \overset{*}{\boldsymbol{\varphi}}{}^{(i)} \cdot \overline{\boldsymbol{T}}^{(i)}\, d\Gamma - \int_{\Gamma_c^{(i)}} \overset{*}{\boldsymbol{\varphi}}{}^{(i)} \cdot \boldsymbol{t}^{(i)}\, d\Gamma \right\}, \end{aligned} \tag{3.1}$$

where $\boldsymbol{f}$ denotes the body force, $\boldsymbol{P}$ is the first Piola–Kirchhoff stress tensor, $\overline{\boldsymbol{T}}$ are the prescribed tractions, $\boldsymbol{t}$ the contact tractions, and superscript (i) indicates body (i) ($i = 1$ or 2). The virtual work equation for the system can then be written as

$$G^{int}(\boldsymbol{\varphi}, \overset{*}{\boldsymbol{\varphi}}) + G^{ext}(\boldsymbol{\varphi}, \overset{*}{\boldsymbol{\varphi}}) + G^{c}(\boldsymbol{\varphi}, \overset{*}{\boldsymbol{\varphi}}) = 0, \tag{3.2}$$

in terms of the contributions from internal and external forces and the work associated with contact tractions

$$G^{c}(\boldsymbol{\varphi}, \overset{*}{\boldsymbol{\varphi}}) = -\sum_{i=1}^{2} \int_{\Gamma_c^{(i)}} \overset{*}{\boldsymbol{\varphi}}{}^{(i)} \cdot \boldsymbol{t}^{(i)}\, d\Gamma. \tag{3.3}$$

Consistent with the contact literature, we will refer to $\gamma_c^{(1)}$ as *the slave contact surface* and to $\gamma_c^{(2)}$ as *the master contact surface*.

3.2. Bulk constitutive model

To describe the bulk behavior, we adopt a model formulated in finite deformation kinematics that accounts for both elastic and viscous phenomena. This model relies upon the theory first developed and presented by Reese and Govindjee Reese and Govindjee (1998). The free energy is decomposed additively into a equilibrium (long-time) strain energy and a non-equilibrium (relaxing) part

$$\Psi = \Psi_{EQ}(\boldsymbol{C}) + \Psi_{NEQ}(\boldsymbol{C}_e), \tag{3.4}$$

where $\boldsymbol{C} = \boldsymbol{F}^T\boldsymbol{F}$ is the right Cauchy–Green tensor based upon the full deformation gradient $\boldsymbol{F}$. In analogy with a classical rheological model, the equilibrium part corresponds to the strain energy in the spring and the viscous part to the energy in the Maxwell element.

The elastic right Cauchy–Green tensor $\boldsymbol{C}_e$ is based on the elastic part $\boldsymbol{F}_e$ of the deformation gradient, stemming from the multiplicative decomposition

$$\boldsymbol{F} = \boldsymbol{F}_e\boldsymbol{F}_i, \tag{3.5}$$

where $\boldsymbol{F}_i$ is the viscous counterpart. As a result, we can write $\boldsymbol{C}_e = \boldsymbol{F}_e^T\boldsymbol{F}_e = \boldsymbol{F}_i^{-T}\boldsymbol{C}\boldsymbol{F}_i^{-1}$.

In our implementation, the strain energy function considered for both the equilibrium and the non-equilibrium part is based

on an Ogden model (Ogden, 1972a,b). This model is known to be polyconvex and to agree well with experimental data for rubber-like materials. The Ogden strain energy function has a volumetric part

$$\Psi^{VOL} = \frac{K}{4}(J^2 - 2lnJ - 1), \tag{3.6}$$

expressed in terms of the Jacobian of the deformation gradient, and a deviatoric part

$$\Psi^{DEV} = \sum_{r=1}^{N} \frac{G_r}{\alpha_r}(\overline{b_1}^{\alpha_r/2} + \overline{b_2}^{\alpha_r/2} + \overline{b_3}^{\alpha_r/2}), \tag{3.7}$$

expressed in terms of the modified principal values of the left Cauchy–Green tensor ($\overline{\boldsymbol{b}} = J^{-2/3}\boldsymbol{b}$). Currently our formulation includes three terms ($N = 3$) in the deviatoric strain energy (3.7) for a total of seven constitutive parameters (G_r and α_r; $r = \overline{1,3}$ and the bulk modulus, K). Note (Ogden, 1972a) that the bulk shear modulus is $G = \sum_{r=1}^{N} \frac{1}{2} G_r \alpha_r$.

The resulting evolution equation is similar in structure to the one used in finite deformation elastoplasticity, where the state determined based on the elastic predictor step is called the "trial" state. This equation introduces two more constitutive parameters, the deviatoric and volumetric viscosities (η_D and η_V).

The assumption of the existence of a free energy for the non-equilibrium stress does not generally hold for any viscoelastic material but seems to be reasonable in the case of rubber-like materials. Our work investigated the accuracy of this assumption for hydrogel materials and confirmed the ability of this model to offer sufficiently good correlation with experimental data when the constitutive parameters are properly calibrated. These parameters can be classified in two groups: (1) *strain energy parameters* including the bulk modulus describing the volumetric behavior and the $2N$ parameters for the description of the deviatoric behavior, and (2) *viscosities* (two parameters, the deviatoric and volumetric viscosity).

3.3. Interfacial constitutive model

To characterize the interfacial behavior, we define the gap vector function, $\boldsymbol{g}$:

$$\boldsymbol{g}(\boldsymbol{X}, t) = \boldsymbol{\varphi}^{(1)}(\boldsymbol{X}, t) - \boldsymbol{\varphi}^{(2)}(\overline{\boldsymbol{Y}}, t), \tag{3.8}$$

where $\overline{\boldsymbol{Y}}$ is the closest point projection of point $\boldsymbol{X}$ onto the master surface, and $\boldsymbol{v}$ the relative velocity between the two surfaces in contact, which can be decomposed into its normal and tangential parts

$$\boldsymbol{v} = \dot{\boldsymbol{\varphi}}^{(2)}(\overline{\boldsymbol{Y}}, t) - \dot{\boldsymbol{\varphi}}^{(1)}(\boldsymbol{X}, t) = \boldsymbol{v}_N + \boldsymbol{v}_T. \tag{3.9}$$

The contact boundary condition in the normal direction $\boldsymbol{n}$ can be represented as an impenetrability condition in the form $\boldsymbol{n} \cdot \boldsymbol{g}(\boldsymbol{X}, t) \leqslant 0$. The norm of the tangential component of $\boldsymbol{v}$ – hereafter referred to as sliding velocity $v_s = \|\boldsymbol{v}_T\|$ – is an important parameter for the characterization of the tribological properties of the interface. Kagata et al. (2002) reported from their experimental studies that at constant sliding velocity the frictional force per unit area (τ) is proportional to $(\sigma_n)^{\alpha}$, where σ_n is the normal contact stress and $\alpha \in [0, 1]$ is a constant. In the limit, the solid (dry) friction law is then obtained for $\alpha = 1$. They have also reported that the frictional force increases with an increase in the sliding velocity but the profile does not correspond to typical forces that would arise from a viscous flow model (i.e., $\propto v_s$). It is in fact dependent on the applied compressive load: at small normal strains it is almost constant at low velocities and has a clear gradual increase in the range of the higher velocities whereas at larger normal strains it has a moderate increase in the range of the low velocities but increases significantly for larger velocities. The dependence on velocity is then less important at small normal strains and velocities but becomes significant at larger normal strains and velocities. The assumption of a dependence of the frictional forces on both σ_n and on the sliding velocity $\tau = \tau(v_s, \sigma_n)$ is therefore suggested by experimental observation. Fig. 4 presents a typical plot of the total torque during an experiment (using the set-up shown in Fig. 1) on hydrogels where the angular velocity (ω) was increased from zero to 10 rad/s over four different steps.

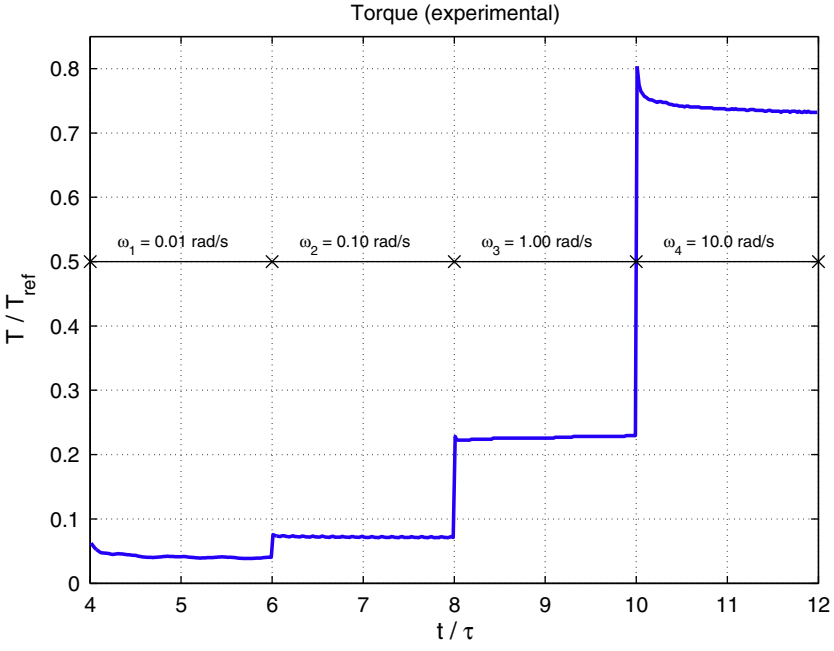

Fig. 4. Measured torque during experiment on hydrogel specimens.

Unfortunately, the direct extraction of the total frictional force is not possible without hypothesizing the form of this dependence, and hence we have no direct indication of what the explicit form of τ should be. In this paper, we have adopted an interface model that decouples this dependence, i.e., $\tau = \mu\sigma_n$ with $\mu = h(v_s)$. In Section 5, we will show how strongly the computationally predicted torque signal depends on the hypothesis for h.

In the examples presented in Section 5, second-order polynomial functions were considered for h, with a maximum of three independent parameters to define the local coefficient of friction in terms of the sliding velocity

$$\mu = h(v_s) = \beta_0 + \beta_1 v_s + \beta_2 v_s^2 = \boldsymbol{\beta} \cdot \mathbf{p}[v_s], \tag{3.10}$$

where $\boldsymbol{\beta} = (\beta_0, \beta_1, \beta_2)^T$ and $\mathbf{p}[v_s] = (1, v_s, v_s^2)^T$.

Following the procedure outlined in Section 2, we can use (3.10) and the measured torque and normal force signals to estimate a *global apparent coefficient of friction*. While such an approach requires many simplifying assumptions, we find it useful to explore here as a means to demonstrate the usefulness/limitations of a purely analytical approach to identifying details of the interfacial constitutive law.

The approach neglects the deformation produced during contact of the two gel cylinders. In this case, the radius of the contact patch can be assumed to be R_{min} (i.e., the minimum radius of the two cylinders in contact), $v_s \sim \omega r$ with r the distance from the rotation axis and ω the angular velocity, and the surface is assumed to remain planar. Analogous to the analysis presented in Section 2, an estimate of the apparent coefficient of friction can be obtained

$$\mu_{apparent} = \left(\frac{\beta_0 \frac{1}{2} + \beta_1 \frac{R\omega}{3} + \beta_2 \frac{R^2\omega^2}{4}}{\beta_0 \frac{1}{3} + \beta_1 \frac{R^2\omega}{4} + \beta_2 \frac{R^3\omega^2}{5}} \right) \frac{T}{N}. \tag{3.11}$$

where T is the torque, N the axial force, and R the radius of the contact surface (under the hypothesis of small deformations $R = R_{min}$). The quadratic polynomial can be generalized to an arbitrary polynomial function of v_s:

$$h = \sum_{i=0}^{n} \beta_i v_s^{v_i}. \tag{3.12}$$

The apparent coefficient of friction in this case can be estimated as

$$\mu_{apparent} = \left(\frac{\sum_i \beta_i \omega_i^{v_i} \frac{R_{min}^{v_i+2}}{v_i+2}}{\sum_i \beta_i \omega_i^{v_i} \frac{R_{min}^{v_i+3}}{v_i+3}} \right) \frac{T}{N}. \tag{3.13}$$

The estimates (3.11) and (3.13) have a limited range of validity due to many factors: the contact surface does not remain planar, the radius of the contact patch $R_{contact} \neq R_{min}$ and the normal tractions are not uniformly distributed. These expressions can be used in practice to obtain estimates of β_0, β_1, and β_2 based on the ratios T/N for a given set of ω. Indeed, we explore the use of least-squares fitting techniques to obtain the coefficients $\boldsymbol{\beta}$ in the numerical studies provided in Section 5.

4. Numerical implementation

4.1. Bulk behavior

The nonlinear viscoelastic constitutive model proposed by Reese and Govindjee (1998) and described in Section 3.2 was implemented in the finite-element program FEAP (Taylor, 2003). The general theory for finite viscoelasticity presented in Reese and Govindjee (1998) reduces in the case of small deformations to the standard theory of infinitesimal viscoelasticity. The split of the strain energy (3.4) into a long time "spring" energy (corresponding to thermodynamic equilibrium) and strain energy in the Maxwell element (non-equilibrium) is closely associated to the multiplicative split of the total deformation gradient (3.5).

The evolution equation based on this operator split is similar in structure to that used in large deformation elastoplasticity. In close analogy, the state predicted by the elastic part is considered a trial state and is followed in the algorithm by an inelastic corrector step. Consequently, following well established techniques in elastoplasticity (Simo, 1992), the viscous update, which consists of integrating the evolution equation, is performed in principal directions by means of the exponential mapping algorithm. The approximate expression used in the implementation is first order accurate. The viscoelastic update of the stresses is calculated at the quadrature points by means of a local Newton iteration and the tangent operator is symmetric. Large loading steps can be robustly handled even though the equations are highly nonlinear. To avoid volumetric locking effects, reduced integration is used for the volumetric stresses for both the equilibrium and non-equilibrium parts. The implementation of this constitutive model in this work includes the non-equilibrium strain energy corresponding to a single Maxwell element.

4.2. Mortar contact formulation with variable friction coefficient

The key idea of a mortar formulation is to project the contact variables on the slave contact surface $\gamma_c^{(1)}$ (Fig. 3) thus obtaining a consistent representation of all variables over a single discretization. These methods enforce the contact constraints in integral form rather than as local constraints (i.e., at the nodes).

The contact virtual work (3.3) is represented in the mortar element formulation as

$$G^m(\boldsymbol{\varphi}, \overset{*}{\boldsymbol{\varphi}}) = -\sum_{i=1}^{2} \int_{\gamma_c^{(i)}} \overset{*}{\boldsymbol{\varphi}}^{(i)} \cdot \boldsymbol{\lambda}^{(i)} \, d\gamma, \tag{4.1}$$

where $\gamma_c^{(i)}$ is the contact surface in the current configuration of body (i) and $\boldsymbol{\lambda}^{(i)}$, further referred as mortar multipliers, are the Cauchy tractions on the contact surface.

Using the balance of contact forces across the interface $\boldsymbol{\lambda}^{(1)} \, d\gamma_c^{(1)} = -\boldsymbol{\lambda}^{(2)} \, d\gamma_c^{(2)}$, Eq. (4.1) can be recast as

$$G^m(\boldsymbol{\varphi}, \overset{*}{\boldsymbol{\varphi}}) = -\int_{\gamma_c^{(1)}} \boldsymbol{\lambda}^{(1)}(\boldsymbol{X}) \cdot (\overset{*}{\boldsymbol{\varphi}}^{(1)}(\boldsymbol{X}) - \overset{*}{\boldsymbol{\varphi}}^{(2)}(\overline{\boldsymbol{Y}})) d\gamma. \tag{4.2}$$

In this framework, the normal contact constraints are expressed via the Kuhn–Tucker conditions:

$$g_N(\boldsymbol{X}, t) \leqslant 0, \tag{4.3}$$

$$\lambda_N(\boldsymbol{X}, t) \geqslant 0, \tag{4.4}$$

$$\lambda_N(\boldsymbol{X}, t) g_N(\boldsymbol{X}, t) = 0, \tag{4.5}$$

where $g_N(\boldsymbol{x}, t) = \boldsymbol{n} \cdot (\overset{*}{\boldsymbol{\varphi}}^{(1)}(\boldsymbol{X}) - \overset{*}{\boldsymbol{\varphi}}^{(2)}(\overline{\boldsymbol{Y}}))$ is the normal component of the gap vector. Frictional contact conditions using Coulomb's law can be added

$$\boldsymbol{v}_T \sim \frac{\boldsymbol{\lambda}_T}{\|\boldsymbol{\lambda}_T\|}, \tag{4.6}$$

$$\|\boldsymbol{\lambda}_T\| - \mu \|\boldsymbol{\lambda}_N\| \leqslant 0, \tag{4.7}$$

enforcing the tangential tractions to be parallel to the direction of the tangent velocity and enforcing Coulomb's law. The mortar (discretized) version of these constraints can then be obtained and integration of all terms is performed on the slave surface. It is apparent that in the context of discretized (faceted) geometry of the contact surface, the discontinuities of the normal and tangent vectors across neighboring facets can impair the robustness of the algorithm. A continuous normal is thus defined using weighted averages. The interested reader is referred to Yang et al. (Yang and Laursen,

2006; Yang et al., 2005) for details on the application of mortar methods to frictional contact problems in the context of large deformations.

We now introduce the use of a mortar contact formulation with *velocity-dependent coefficient of friction* for the analysis of the surface behavior of soft wet materials. Eq. (3.12) makes the coefficient of friction local, and dependent on the current solution. In the context of the Newton–Raphson solution method used to solve the nonlinear system, the coefficient of friction is *evaluated at each node* on the contact patch and *updated in each Newton–Raphson iteration*. The frictional contact conditions are now expressed as

$$\boldsymbol{v}_T \sim \frac{\boldsymbol{\lambda}_T}{\|\boldsymbol{\lambda}_T\|}, \tag{4.8}$$

$$v_s = \|\boldsymbol{v}_T\|, \tag{4.9}$$

$$\|\boldsymbol{\lambda}_T\| - \mu(v_s)\|\boldsymbol{\lambda}_N\| \leqslant 0. \tag{4.10}$$

To evaluate the contribution of the frictional force to the total force vector, numerical integration is utilized. At each quadrature point on the contact patch, we first determine the relative sliding velocity using the element shape functions and nodal velocities. The coefficient of friction is then evaluated using (3.12). We note that in order to keep the optimal (quadratic) convergence rate in the Newton–Raphson iteration, linearization of the coefficient of friction is necessary since it depends on the current configuration through the sliding velocity.

5. Numerical experiments

Due to the nature of the experiments from which data were available, the examples presented in this section are all numerical simulations of axisymetric problems. However, the finite element formulations for the viscoelastic bulk behavior and for the frictional contact were implemented using three-dimensional domains partitioned into eight-node linear brick elements. All results provided represent spatially-converged numerical approximations to the solution of the associated boundary-value problem.

5.1. Bulk behavior

We select constitutive parameters for the model described in Section 3.2 that yield a bulk response in uniaxial compression, torsion, and relaxation representative of gel-like materials. The parameters are listed in Table 1. These parameters were found to provide an excellent match to data for the uniaxial compression/stress relaxation of the hydrogels studied in Chang et al. (2007). For the purpose of this investigation, the important point is that the surface deformation is expected to compare favorably to that present in the tribological studies of Chang et al. (2007).

Table 1
Baseline material properties and parameters used in the numerical studies. Quantities are given using N, m, s units.

Elastic moduli								
Property	G_1	α_1	G_2	α_2	G_3	α_3	K	
Value	7.5e^5	1.3	0.45	2	0.18	5	2.0e^5	
Viscous moduli								
Property	G_{1v}	α_{1v}	G_{2v}	α_{2v}	G_{3v}	α_{3v}	η_d	η_v
Value	2.5e^5	1.3	0.45	2	0.18	5	4.5	200

The viscoelastic relaxation behavior of the bulk can be captured through simulations where the load is first applied and then held fixed during the subsequent relaxation. We show here typical results from such a simulation, where both the normal force relaxation and the torque relaxation are accounted for. The simulation proceeds as follows. A cylindrical body is first compressed axially, then undergoes a relaxation of the normal force, then torque is applied at $t = 3600$ s followed by the corresponding torque relaxation step. Fig. 5 presents the relaxation of the normal force and torque during the four-step simulation (initial compression and relaxation followed by subsequent application of the torque and the corresponding relaxation). The time axis is normalized by $\tau = 3600$ s (the total time of the normal loading plus the normal relaxation), the normal force is normalized by the long-time value at the end of the simulation (hereafter referred to as N_{ref}), and the torque is normalized by $T_{ref} = N_{ref}R$, where R is the radius of the smallest cylinder. We note that the normal force increases when the torque is applied due to nonlinear Poisson effects.

5.2. Hydrogel to hydrogel friction. Estimate of the apparent coefficient of friction

We provide results from simulations based on the setup and geometry shown in Fig. 1, using dimensions based on the experimental work of Chang et al. (2007). Specifically, a cylinder with radius $R_{min} = 10$ mm is fixed at the upper base and placed above a cylinder with radius $R_{max} = 12.5$ mm, which is fixed at the lower base.

All simulations described in the remainder of this section are based on the following load sequence: a compressive load is applied incrementally in the time interval $t \in [0, 27\ \text{s}]$ as the two cylinders are brought into contact. The compression is then held fixed

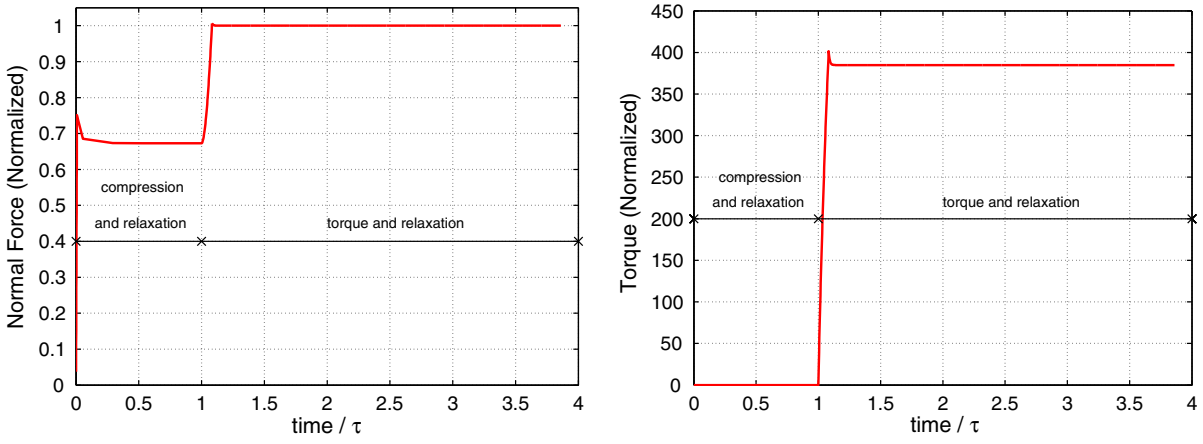

Fig. 5. Resultant normal force (left) and torque (right) predicted by simulation of relaxation experiment for hydrogel-on-hydrogel compression followed by torsion.

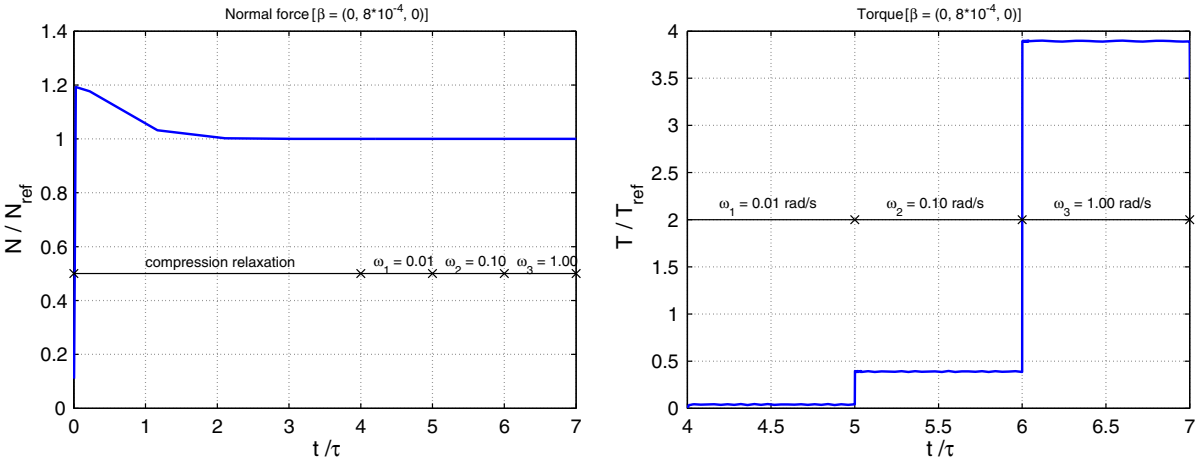

Fig. 6. Resultant normal force (left) and torque (right) predicted by mortar-finite element simulation of rotational contact between two cylindrical hydrogel specimens. The coefficient of friction is taken to be linearly proportional to the relative sliding velocity as $\mu = 8 \cdot 10^{-4} v_s$.

over an interval $t = 3600$ s for the material to reach the long-term behavior after relaxation. Rotation of the top surface is then applied, in three successive steps of 900 s each:

$$\omega_1 = 0.01 \text{ rad/s}, \quad t \in [3600, 4500]\text{s},$$
$$\omega_2 = 0.10 \text{ rad/s}, \quad t \in [4500, 5400]\text{s},$$
$$\omega_3 = 1.00 \text{ rad/s}, \quad t \in [5400, 6300]\text{s}.$$

Frictional slip at the contact surface gives rise to a resultant torsion T.

Typical results for the axial force and the torque are presented in Fig. 6. The time axis is normalized by $\tau = 900$ s (the duration of an interval at a given rotation speed). N_{ref} is the long time value of the axial force and $T_{ref} = N_{ref} R_{min}$. The results correspond to a coefficient of friction that is linearly proportional to the relative sliding velocity through $\mu = 8 \cdot 10^{-4} v_s$, or $\boldsymbol{\beta} = (0, 8 \cdot 10^{-4}, 0)$. Qualitatively the plots present the same behavior observed in the experimental data: the axial force is approximatively constant when rotation is applied, and the torque presents step jumps at the variation of ω. Quantitatively, we will show that the values are strongly dependent on the choice one makes for the function describing the friction law.

Based on (3.11) and using the normal force and torque results that are predicted numerically, an estimate of the global apparent coefficient of friction is computed and presented in Fig. 7. For comparison we also show the mean value and a weighted average value (using quadrature weights) of the converged coefficient of friction calculated over the numerical contact patch. It can be seen that (3.11) slightly overestimates the converged weighted values. Recall (Section 3.3) that the analytical estimate Eq. (3.11) is obtained under the simplifying assumption of small deformations: the contact patch surface is assumed to remain planar and of constant radius R_{min}. The deformed configuration obtained under the described loading, however, places the system outside the range

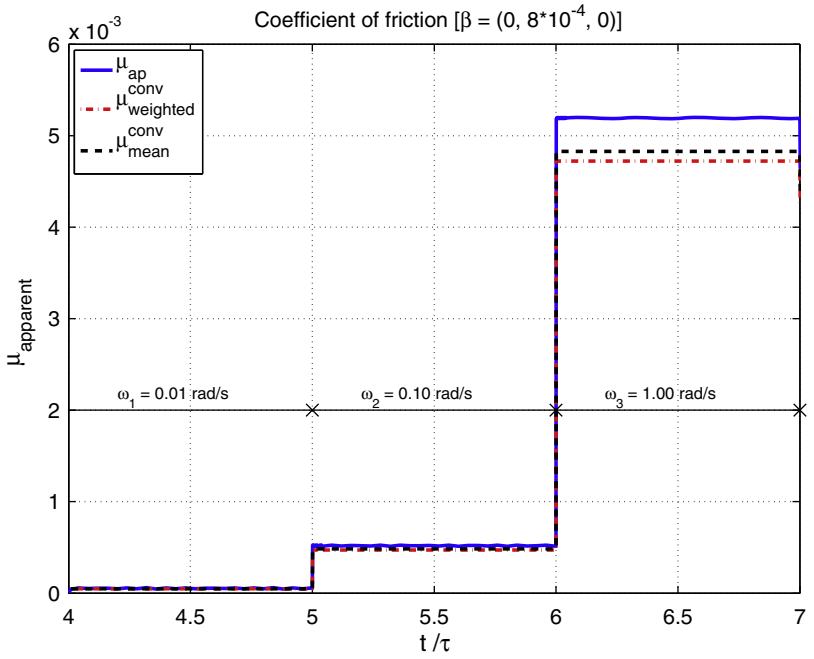

Fig. 7. Estimate of the global coefficient of friction as a function of time, using $\mu = 8 \cdot 10^{-4} v_s$.

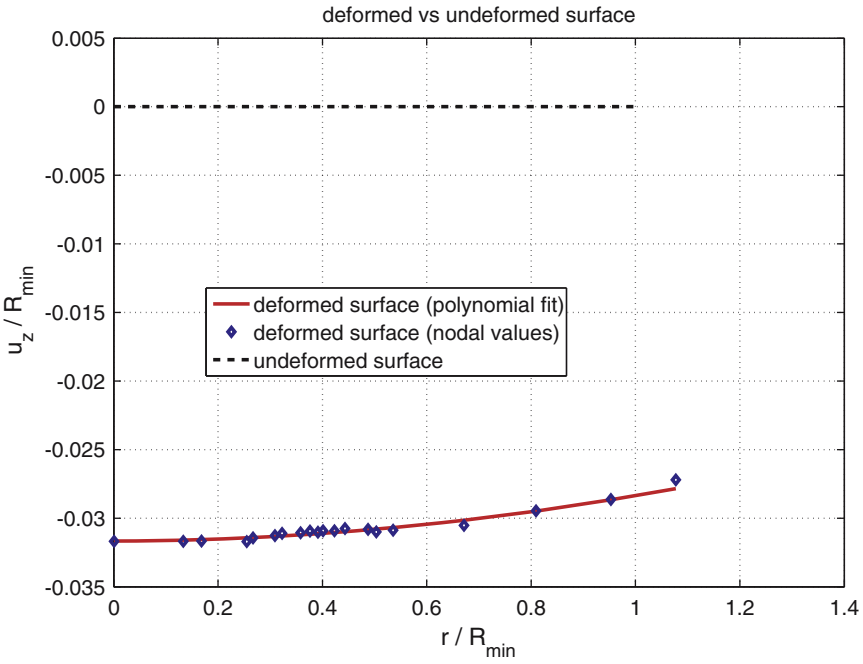

Fig. 8. Undeformed and deformed configurations along a radial line in the contact patch.

Table 2
Parameters describing the interfacial laws.

Case	β_0	β_1	β_2
1	0	$2 \cdot 10^{-4}$	0
2	$2.6 \cdot 10^{-4}$	0	$1 \cdot 10^{-5}$
3	$2.2 \cdot 10^{-4}$	$3.26 \cdot 10^{-5}$	0

where these assumptions are reasonable. We show in Fig. 8 the deformed configuration of the contact patch. As it can be seen, the surface does not remain planar, in fact the vertical displacement of the outer nodes on the contact patch is 0.12338 mm while the displacement of the center nodes is 0.31151 mm. The radius of the horizontal projection of the contact patch also increases significantly, from $R_{min} = 10$ mm to $R_{contact} \sim 10.9$ mm.

In order to extract the coefficients of the interfacial constitutive law from experimental data, one has first to make a hypothesis on the terms that are present in the friction law. For example, one assumes that the law is linear in the sliding velocity, i.e., $\mu = \beta_1 v_s$. Then a least squares technique is used that allows for calculation of the best β_1. Similarly, one can assume another form of the law, say quadratic, and obtain a "best fit" for β_2. In what follows, we present the results of several simulations performed with various $\boldsymbol{\beta} = (\beta_0, \beta_1, \beta_2)$ (values for all cases are listed in Table 2 and the cor-

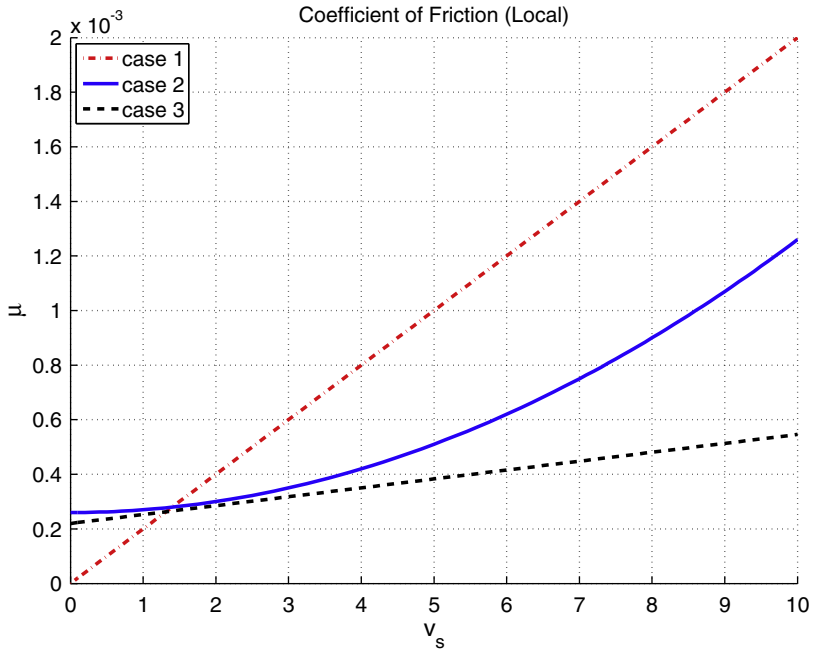

Fig. 9. Interfacial laws used for comparison.

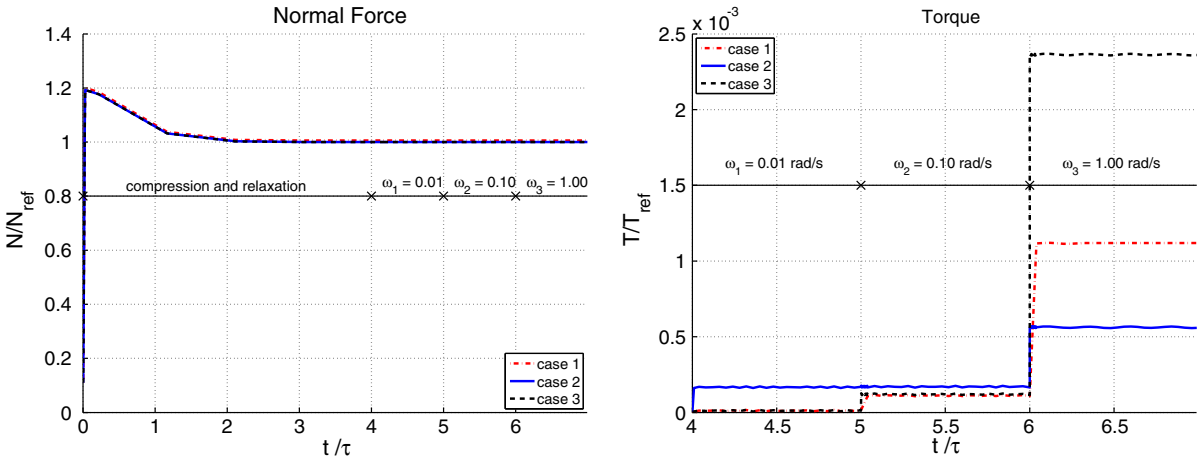

Fig. 10. Total normal force (left) and torque (right) predicted by mortar-finite element simulations for various choices of the frictional parameters β.

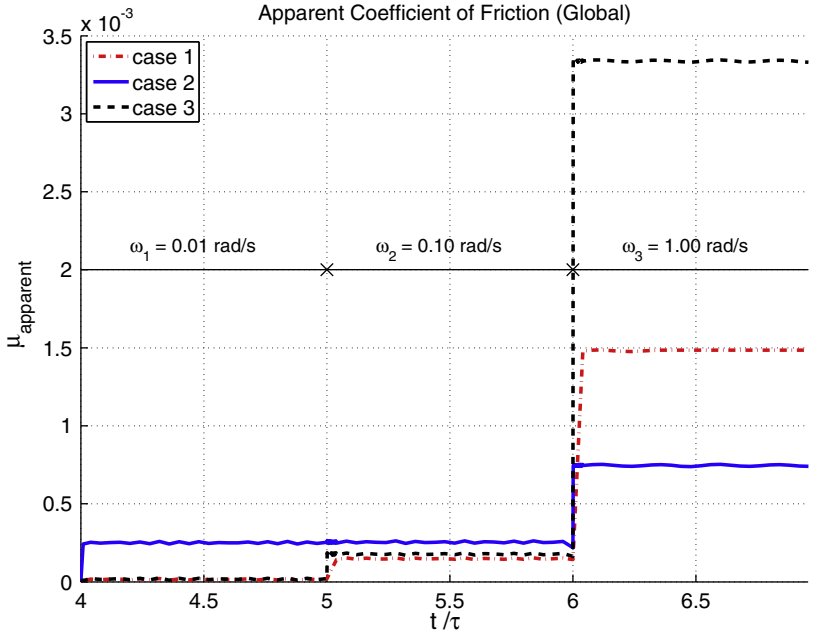

Fig. 11. Estimate of the global coefficient of friction for various interfacial constitutive laws. Each case of β constitutes a different fit to the same experimental data.

responding plots of the local μ variation are shown in Fig. 9). These simply represent different polynomial expansions that are meant to roughly represent the same trends. Unfortunately, as it is shown in Figs. 10 and 11, that initial assumption on the form of the independent terms one introduces in the law has a strong influence on the results obtained.

The computational model has a good level of fidelity in capturing the jumps corresponding to changes in ω but at the same time it is very sensitive to the choice of the interfacial constitutive law. Identification of the friction law based on experimental data is not a trivial task for this application. This is due to the fact that the typical rheometer experiment offers access to information about global quantities (like the normal force and total torque) whereas the friction law we look for is local in nature. Fig. 10 shows (as expected) that the variation of the axial load is not dependent upon the change in the friction coefficient, while the torque is strongly dependent on β. Consequently, this influence is also observed in the estimate of the apparent coefficient of friction shown in Fig. 11. Note that, for normalization, we have used the long time values of N corresponding to each individual simulation.

A comparison with the behavior of the system neglecting the viscous terms in the bulk in either the top or bottom specimen (or both) was also performed and the results (normal force, torque, apparent coefficient of friction) are shown in Fig. 12 and 13. The friction law considered in this case was $\mu = 0.0015 \cdot v_s + 10^{-5} \cdot v_s^2$. Contact was considered for the following cases: viscoelastic to viscoelastic, hyperelastic to viscoelastic and hyperelastic to hyperelastic. It can be seen that, as expected, the steady state (long term) values of the torque, normal force and apparent coefficient of friction are independent of the model.

However, the relaxation behavior of the material itself cannot be captured if a hyperelastic model is used. Depending on the purpose of the simulation, if only long term friction properties need to be extracted one can conclude that a simple hyperelastic material model may be more efficient computationally. If the bulk behavior

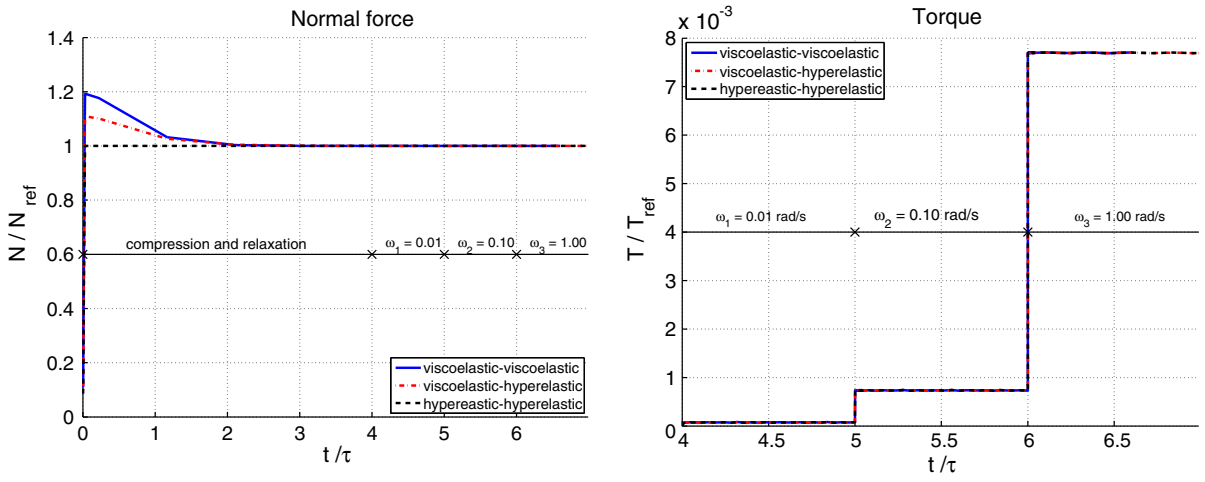

Fig. 12. Total normal force (left) and torque (right) predicted by mortar-finite element simulations, neglecting viscous terms in the bulk constitutive law for either one or both of the gel samples in contact.

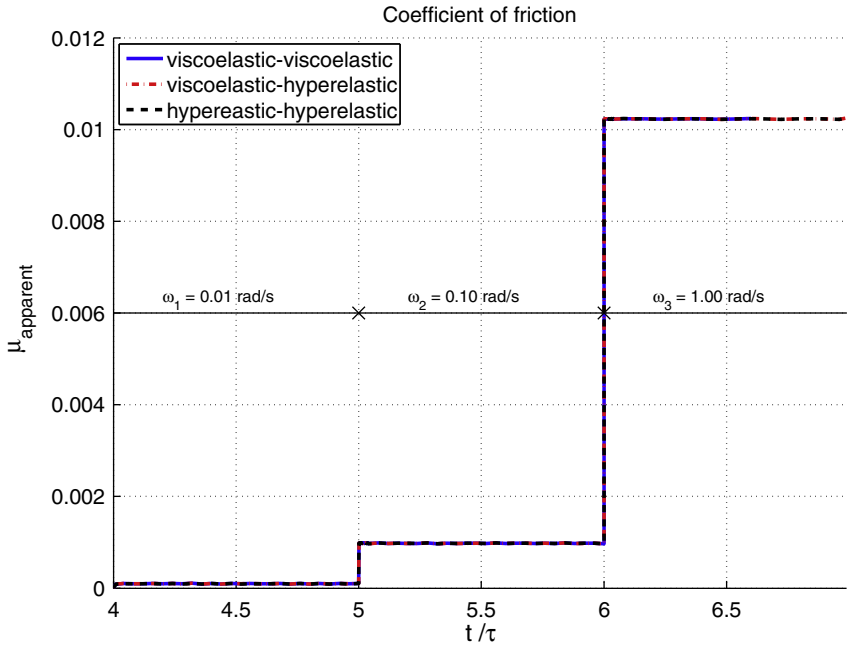

Fig. 13. Estimate of the global coefficient of friction for the bulk constitutive study.

needs to be captured, the computational price has to be paid and a viscoelastic model should be used.

6. Conclusions

In this paper, a finite element formulation for the analysis of surface phenomena in soft-wet materials has been presented. Based upon experimental observations, the frictional phenomena on the contact surface was modeled under the assumption of a coefficient of friction dependent on the relative sliding velocity. To this end, a mortar contact method with variable coefficient of friction was formulated and implemented. The computational approach we propose has been shown to have a good level of fidelity in capturing the surface behavior, and the numerical results are strongly dependent on the chosen frictional law. In fact, the reliance of the solution on the hypothesized interfacial constitutive model is a key aspect here as we have shown that several choices with constitutive parameters calculated to fit the same experimental data set lead to substantially different numerical predictions. This is due to the fact that the fitting technique requires an assumed shape for the dependence and is therefore biased by this choice. The recovery of the interfacial constitutive model from experimental data is beyond the scope of this paper and is the subject of future work.

Acknowledgement

This material is based upon work supported by the National Science Foundation under Grant No. CMMI 0324459. This support and the collaboration of Ms. Debby Chang who provided the experimental data are greatly appreciated.

References

Bassetti, M.J., Chatterjee, A.N., Aluru, N.R., Beebe, D.J., 2005. Development and modeling of electrically triggered hydrogels for microfluidic applications. Journal of Microelectromechanical Systems 14 (5), 1198–1207.

Baumberger, T., Caroli, C., Ronsin, O., 2002. Self-healing slip pulses along a gel/glass interface. Physical Review Letters 88 (7).

Beebe, D.J., Moore, J.S., Bauer, J.M., Yu, Q., Liu, R.H., Devadoss, C., Jo, B., 2000. Functional hydrogel structures for autonomous flow control inside microfluidic channels. Nature 404, 588–590.

Chang, D., Dolbow, J.E., Zauscher, S., 2007. Switchable friction of stimulus-responsive hydrogels. Langmuir 23, 250–257.

Dolbow, J., Fried, E., Ji, H., 2004. Chemically induced swelling of hydrogels. Journal of the Mechanics and Physics of Solids 52, 51–84.

Eichenbaum, G.M., Kiser, P.F., Shah, D., Simon, S.A., Needham, D., 1999. Investigation of the swelling response and drug loading of ionic microgels: the dependence on functional group composition. Macromolecules 32, 8996–9006.

Gong, J., Kagata, G., Osada, Y., 1999. Friction of gels. 4. Friction on charged gels. Journal of Physical Chemistry B 103 (29), 6007–6014.

Hong, W., Zhao, X., Zhou, J., Suo, Z., 2008. A theory of coupled diffusion and large deformation in polymeric gels. Journal of the Mechanics and Physics of Solids 56 (5), 1779–1793.

Kagata, G., Gong, J., Osada, Y., 2002. Friction of gels. 6. Effects of sliding velocity and viscoelastic responses of the network. Journal of Physical Chemistry B 106 (18), 4596–4601.

Korchagin, V., Dolbow, J., Stepp, D., 2007. A theory of amorphous viscoelastic solids undergoing finite deformations with application to hydrogels. International Journal of Solids and Structures 44, 3973–3997.

Li, H., Luo, R., Birgersson, E., Lam, K.Y., 2007. Modeling of multiphase smart hydrogels responding to ph and electric voltage coupled stimuli. Journal of Applied Physics (11), 101.

McDevitt, T., Laursen, T.A., 2000. A mortar-finite element formulation for frictional contact problems. International Journal of Numerical Methods in Engineering 48 (10), 1525–1547.

Ogden, R.W., 1972a. Large deformation isotropic elasticity – on the correlation of theory and experiment for compressible rubber-like solids. Proceedings of the Royal Society London A (328), 567–583.

Ogden, R.W., 1972b. Large deformation isotropic elasticity – on the correlation of theory and experiment for incompressible rubber-like solids. Proceedings of the Royal Society London A (326), 565–584.

Onuki, A., 1993. Theory of phase transition in polymer gels. In: Dušek, K. (Ed.), Responsive Gels: Volume Transitions I, Advances in Polymer Science, vol. 109. Springer, Berlin, pp. 63–121.

Osada, Y., Gong, J.P., 1999. Soft and wet materials: polymer gels. Advanced Materials 10, 827–837.

Pardo-Yissar, V., Gabai, R., Shipway, A.N., Bourenko, T., Willner, I., 2001. Gold nanoparticle/hydrogel composites with solvent-switchable electronic properties. Advanced Materials 13, 1320–1323.

Reese, S., Govindjee, S., 1998. A theory of finite viscoelasticity and numerical aspects. International Journal of Numerical Methods in Engineering 35 (26–27), 3455–3482.

Simo, J.C., 1992. Algorithms for static and dynamic multiplicative plasticity that preserve the classical return mapping scheme of the infinitesimal theory. Computer Methods in Applied Mechanics and Engineering 99, 61–112.

Taylor, R.L., 2003. A finite element analysis program, version 7.5.

Yang, B., Laursen, T.A., 2006. A contact searching algorithm including bounding volume trees applied to finite sliding mortar formulations. Computational Mechanics, online, doi:10.1007/s00466-006-0116-z.

Yang, B., Laursen, T.A., Meng, X., 2005. Two dimensional mortar contact methods for large deformation frictional sliding. International Journal of Numerical Methods in Engineering 62 (9), 1183–1225.